Title	Anisotropy resolved multidimensional emission spectroscopy (ARMES): A new tool for protein analysis
Author(s)	Groza, Radu Constantin; Ryder, Alan G.; Li, Boyan
Publication Date	2015-07-30
Publication Information	Groza, RC; Li, BY; Ryder, AG; (2015) 'Anisotropy resolved multidimensional emission spectroscopy (ARMES): A new tool for protein analysis'. Analytica chimica acta, 886 :133-142.
Publisher	Elsevier
Link to publisher's version	http://dx.doi.org/10.1016/j.aca.2015.06.011
Item record	http://hdl.handle.net/10379/5507
DOI	http://dx.doi.org/10.1016/j.aca.2015.06.011

.

Anisotropy Resolved Multidimensional Emission Spectroscopy (ARMES): *a new tool for protein analysis.*

Radu Constantin Groza,   Boyan Li, and Alan G. Ryder.*
Nanoscale BioPhotonics Laboratory, School of Chemistry, National University of Ireland, Galway, Galway, Ireland.

* Corresponding author: **Email:** alan.ryder@nuigalway.ie, **Phone:** +353-91-492943.
Postal address: Nanoscale Biophotonics Laboratory, School of Chemistry, National University of Ireland, Galway, University Road, Galway, Ireland.

Running Title: Protein analysis using multidimensional fluorescence anisotropy.

Abstract:
Structural analysis of proteins using the emission of intrinsic fluorophores is complicated by spectral overlap. Anisotropy resolved multidimensional emission spectroscopy (ARMES) overcame the overlap problem by the use of anisotropy, with chemometric analysis, to resolve the emission of each fluorophore. Total synchronous fluorescence scan (TSFS) provided information about all the fluorophores that contributed to emission while anisotropy provided information about the mobility of each fluorophore. Here the utility of ARMES was demonstrated via study of the chemical and thermal denaturation of human serum albumin (HSA).

Multivariate curve resolution (MCR) analysis of the constituent polarized emission ARMES data resolved contributions from *four* emitters: fluorescence from tryptophan (Trp), solvent exposed tyrosine (Tyr), Tyr in a hydrophobic environment, and room temperature phosphorescence (RTP) from Trp. The MCR scores, anisotropy, and literature validated these assignments and showed all the expected transitions during HSA unfolding. This new methodology for comprehensive intrinsic fluorescence analysis of proteins is applicable to any protein containing multiple fluorophores.

Keywords: Fluorescence, Anisotropy, Multidimensional, Protein, Unfolding, Chemometrics.

.

1. Introduction.

Rapid, accurate characterization of macromolecule structure, stability, and aggregation is a critical/challenging task in analytical science. To provide real time information regarding protein stability, the analytical method should be rapid, require a minimum of sample handling and provide high-information content. Spectroscopic methods can fulfil most of these requirements and fluorescence spectroscopy is widely used [1-5]. The use of intrinsic fluorescence is attractive because it facilitates analysis of proteins in their native state without the use of extrinsic labels, which involves additional sample manipulation and may also change macromolecule structural/chemical properties. For example, the hydrodynamic radius of HSA at 25 °C was variously reported to be between 31.5 and 35.6 Å [6-8] in the native state, and 39.1±2.5 Å with a TMR label [9].

One of the most widely studied and important proteins involved in human health is HSA because of its abundance and role as a transport protein [10-12]. HSA is comprised of 585 amino acid residues of which phenylalanine (Phe), tryptophan (Trp), and tyrosine (Tyr) are fluorescent [13, 14]. Structurally HSA is composed of three similar α-helical domains I-III, each with a pair of subdomains A and B (*See Supplementary information (SI), Fig. S-1*) [15]. A single Trp, Trp-214, located in subdomain IIA dominates emission [16]. Intrinsic fluorescence has been widely used to monitor structural changes in HSA (steady-state or time-resolved emission, or anisotropy) [16-19]. These studies have shown that when thermally denatured, intermediate unfolded states were observed, and that each domain unfolded independently [9, 17, 20]. After thermal denaturation at 50–60 °C, refolding on cooling lead to less stable, native like structures. Above 60°C, unfolding became irreversible, so that when cooled, HSA refolded into structures different from the native state [17, 18, 20, 21].

Multidimensional fluorescence spectroscopy (MDF) techniques, like excitation-emission matrix (EEM) [22] and TSFS [23], have been successfully used for simultaneous analysis of multi-fluorophore mixtures for a wide range of applications [24-28]. In MDF spectroscopy, the data map generated is in essence a spectral fingerprint of the multiple fluorophores present in a protein or a complex sample [26, 28]. HSA fluorescence comprises of overlapping emission from 31 Phe, 1 Trp, and 18 Tyr residues. Fluorophore spectral properties are influenced by a variety of factors linked to protein structure, *e.g.* Förster resonance energy transfers (FRET), electron transfer quenching by peptide bonds, variable solvent exposure, and inner filter effects (IFE) [29, 30]. More specifically the precise fluorophore location and separation between fluorophores and quenchers are the critical parameters. The combination of all these factors determines the gross topography of the emission space and thus generates a unique MDF spectrum. The use of EEM for observing HSA structural changes during freezing has been demonstrated [31, 32], but multivariate analysis was not used to better understand the observed spectral changes in terms of the individual fluorophores.

One of the main problems with fluorescence spectroscopy in general is that the broad excitation and emission bands result in extensive spectral overlap between the chromophores and fluorophores in complex mixtures. Chemometric techniques can be used to resolve

.
contributions and extract relevant and useful analytical information from complex MDF data [33]. Broadly speaking, there are three major approaches to MDF data analysis. First, use multi-way versions of principal component analysis (PCA) to assess how spectra differ. Second, use supervised regression based methods to correlate the observed spectral variations with useful variables like concentration. Third, use multi-way decomposition methods like multivariate curve resolution (MCR) [34-37], parallel factor analysis (PARAFAC) [38-40]. MCR and PARAFAC are used to identify the spectral contributions of individual constituents, which can then be associated with specific fluorophore emission, and component scores can be correlated with concentration. However, even with chemometric analysis, the emission is often not resolvable, so one has to examine the use of other properties to facilitate fluorophore resolution. Combining anisotropy with MDF [41] enabled the differentiation and quantification of fluorophores (protein from free amino acids) with similar emission properties in complex mixtures, based on their rotational speed and hydrodynamic volume, and thus the molecular size, or for macromolecules the mobility/flexibility of the constituent fluorophores.

However, in the course of that study, we noted that in multi-fluorophore proteins like BSA and HSA, anisotropy was not constant across the full emission space. This 4D data generated by *aniso*-TSFS (excitation wavelength (λ_{ex}), wavelength offset ($\Delta\lambda$), intensity (I), anisotropy (r)) from proteins was not easy to understand or interpret. To develop a robust analytical methodology for the quantitative analysis of this unusual *aniso*-TSFS data we took a well-known macromolecule, HSA, which could be reproducibly varied structurally via simple thermal and chemical denaturation. Chemometric methods had then to be evaluated and developed because while there was some available literature on 4-way data analysis [42, 43], none involved fluorescence anisotropy/polarization.

Comprehensive *Aniso*-TSFS data were collected from HSA solutions, which have been subjected to both thermal and chemical denaturation. We looked first at the constituent polarized spectral data using MCR to identify each emitter, and then determined how each individual constituent emitter (both fluorescent and phosphorescent) behaved in the different polarization states in terms of spectral emission and contribution. From this, an initial protein-unfolding model was generated that agreed with the extensive HSA literature. Second, we validated the unfolding model by calculating the anisotropy values and *aniso*-TSFS plots assessing how each emitter behaved in terms of mobility/accessibility changes. It was this combination of methods that provided a unique and very comprehensive picture of how each intrinsic fluorophore was affected by protein structural change. This unique combination of anisotropy, MDF measurements, and factor-based chemometrics was termed "anisotropy resolved multidimensional emission spectroscopy" (ARMES).

2. Materials and Methods

2.1 Materials: HSA (>99%, essentially globulin free), guanidine hydrochloride GuHCl (>99%), sodium sulphite (>98%) and phosphate buffer saline (PBS) tablets were purchased from Sigma-Aldrich. Potassium iodine was purchased from Riedel-deHaën. All compounds were used without further purification. PBS HSA stock solutions were prepared using sterilized high purity water and were membrane filtered (0.22 µm). All stock solutions were stored at –70 °C and defrosted overnight at 4 °C before aliquoting. For thermal denaturation

.

studies (10–70 °C, at 10 °C increments), a 1 mg mL^{-1} HSA solution was used. For HSA chemical unfolding at 25 °C, appropriate amounts were used to prepare 1 mg mL^{-1} HSA solutions with 0–4 M GuHCl concentrations (0.5 M steps). For the room temperature phosphorescence (RTP) validation, 5 M KI (0.18 mL) and 2 M Na$_2$SO$_3$ (0.36 mL) were added to 3 mL (1 mg mL^{-1}) HSA solution to induce the "heavy atom" effect and chemical deoxygenation respectively, and then *aniso*-TSFS measurements made at 10, 20, and 30 °C [5].

2.2 Fluorescence instrumentation and data collection: Spectra were measured in triplicate from solutions in 1×1 cm quartz cuvettes using an Eclipse Fluorescence Spectrophotometer (Agilent) fitted with a manual polarizer accessory and a temperature-regulated single cell cuvette holder (Quantum Northwest). TSFS data were collected over an excitation range of λ_{ex} = 270–370 nm and $\Delta\lambda$ interval of 20–150 nm (2 nm step increments in each case) with 10 nm excitation/emission slit widths (unless otherwise stated) [41]. For each sample, four differently polarized spectra were collected: vertical-vertical (VV), vertical-horizontal (VH), horizontal-vertical (HV) and horizontal-horizontal (HH) which took ~30 minutes per sample. Anisotropy (*r*) at each emission wavelength was calculated using the standard anisotropy formula [1], which was then used to construct *aniso*-TSFS plots. Accurate calculations required that a reasonable intensity be recorded for each of the four polarization spectra [41]. When spectral intensity dropped below the 10% threshold, anisotropy values generally became unreliable with abnormally high or negative *r* values (*vide infra*).

Chemometric methods: Data analysis was performed using MATLAB (ver. 7.0.1), PLS_Toolbox4.0$^{®}$, and in-house written codes. All data were organised with $\Delta\lambda$ (mode 1), λ_{ex} (mode 2), and the sample as mode 3. Datasets had dimensions of 66×51×24 (thermal) and 66×46×27 (chemical) respectively. Spectral variance, and number of factors, were first assessed using NPFPCA (noise perturbation in functional principal component analysis) which is a variant form of the functional PCA better suited to noisy data [44, 45]. NFPCA makes use of systematic noise effects and the addition of synthetic noise to produce more reliable results. It then implemented PCA, which relies just on the existing random effect in the data to identify representative eigenvectors. Multi-way decomposition was performed using MCR alternating least squares (ALS) where models were constructed on the augmented matrix datasets with $\Delta\lambda$ as the 'spectral' mode and the 'λ_{ex}×sample' as the 'concentration' mode. Mode 1 loadings represent the 'delta' profiles while mode 2 loadings represent component excitation profiles/spectra.

3. Results and Discussion

3.1 Spectroscopic Analysis: ARMES first required the accumulation of four separate polarization datasets (HH, VV, VH and HV) and the first thing of note was that the polarized emission intensity of HSA was approximately an order of magnitude lower than standard TSFS measurements (*Supplemental information, Fig. S-2*) which caused a significant reduction in signal-to-noise ratio (SNR). HH and VV spectra were more intense compared to HV and VH due to the more rigid fluorophore environment. HH spectra were always more intense than the VV, because of the better transmittance of the filters in this orientation (see *Figure S-3*). For HSA, strong emission from Trp and Tyr were observed over λ_{ex}=280–320 nm and $\Delta\lambda$=20–140 nm ranges (corresponding to λ_{ex}=280–320 nm, λ_{em}=300–460 nm EEM

.

ranges). A weaker broad band (λ_{ex}= 290–370/$\Delta\lambda$= 40–150 nm), corresponding to emission band maxima at 444 nm (HH/VH) and 454–460 nm (VV/HV) spectra was ascribed to Trp–214 RTP (*vide infra*).

TSFS spectra and the constituent emission and excitation maxima were all significantly red-shifted. This was because most standard fluorescence spectrometers (as used here) have polymer thin film polarizers for anisotropy measurements and these typically cut-off below 290–300 nm (*SI, Fig. S-3*) which resulted in distorted MDF spectra. This caused the excitation maxima of the recovered components to be red-shifted by amounts that were equal to the real excitation maximum plus the spectral distance to the cut-off point. For TSFS, emission maxima ($\lambda_{ex}+\Delta\lambda$) were also shifted towards longer wavelengths by the same spectral distance as the excitation maxima. This also reshaped the polarized TSFS spectra compared to non-polarized spectra (*SI, Fig. S-4*). One advantage of this effect is that it compensated for the lack of tri-linearity in TSFS data which facilitated reliable component recovery using MCR (*vide infra*).
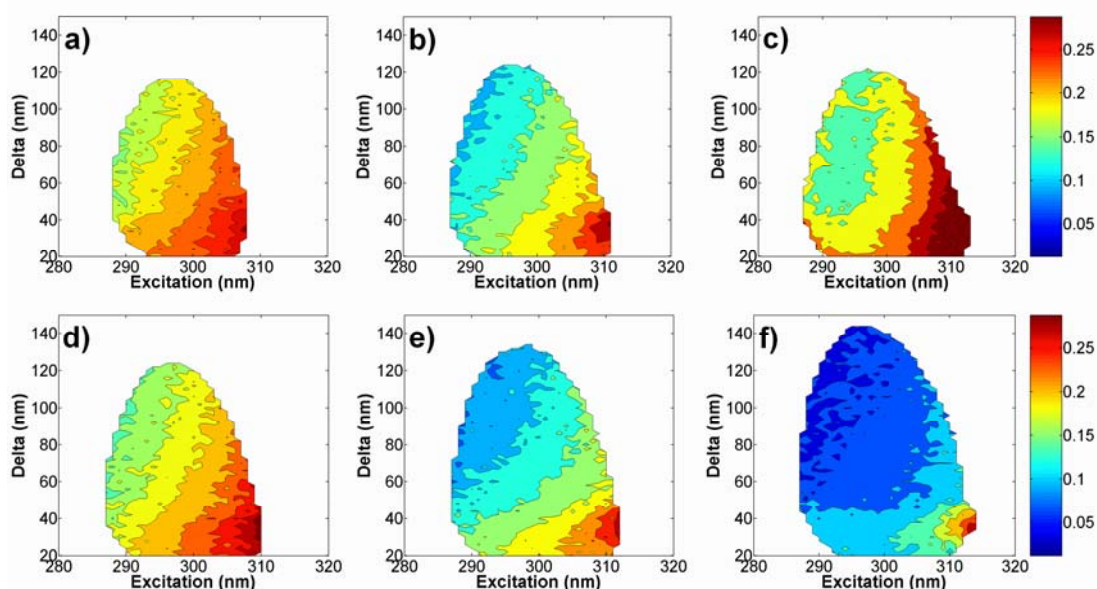

Figure 1: Changes in the *aniso*-TSFS contour plots for HSA 1mg mL^{-1} in PBS undergoing thermal unfolding: *a)* 10 °C, *b)* 50 °C, and *c)* after cooling from 70→20 °C, and chemical unfolding at 20 °C with: *d)* 0 M, *e)* 2 M, and *f)* 4 M GuHCl. The color bar on the right represents anisotropy.

Aniso-TSFS plots (Figure 1) have a distinct striped pattern, which highlighted the significant anisotropy variation across the emission space. This was due to numerous factors including: fluorophore type and number, variability in mobility of fluorophores located in different protein domains, variations in intra-molecular FRET, and changing local chemical environment. In contrast, *aniso*-TSFS plots of simple fluorophores with single state emission show constant anisotropy values across the entire emission space [41]. HSA *aniso*-TSFS patterns were very different for thermal compared to chemical denaturation because of the different unfolding pathways. Univariate analysis of average anisotropy values (*SI, Fig. S-5*) did not adequately explain which fluorophores contributed to the anisotropy and pattern changes.

.

3.2 Chemometric analysis: To identify which fluorophores generated the *aniso*-TSFS changes, MCR was undertaken on the raw (HH/VV/HV/VH) and *aniso*-TSFS data. NPFPCA first estimated the number of principal components in the augmented datasets. This showed that there were always four significant components (*i.e.* fluorophores) present in all four differently polarized datasets, which always explained >99% of the data variance (*SI, Table S-1*). MCR modelling using a confidence level of 0.95, non-negativity constraints, and typically 100 iterations, was repeated three times on each individual replicate set of measurements (no benefit was seen from undertaking more iterations). This yielded emission and excitation profiles (Figure 2), and the scores (confidence intervals calculated from the three replicate measurements) for each component (Figure 3) which were used to generate reconstructed TSFS/EEM spectra of the individual components (*SI, Fig. S-6*) as well as the relative contribution of each fluorophore to each measured polarization state.
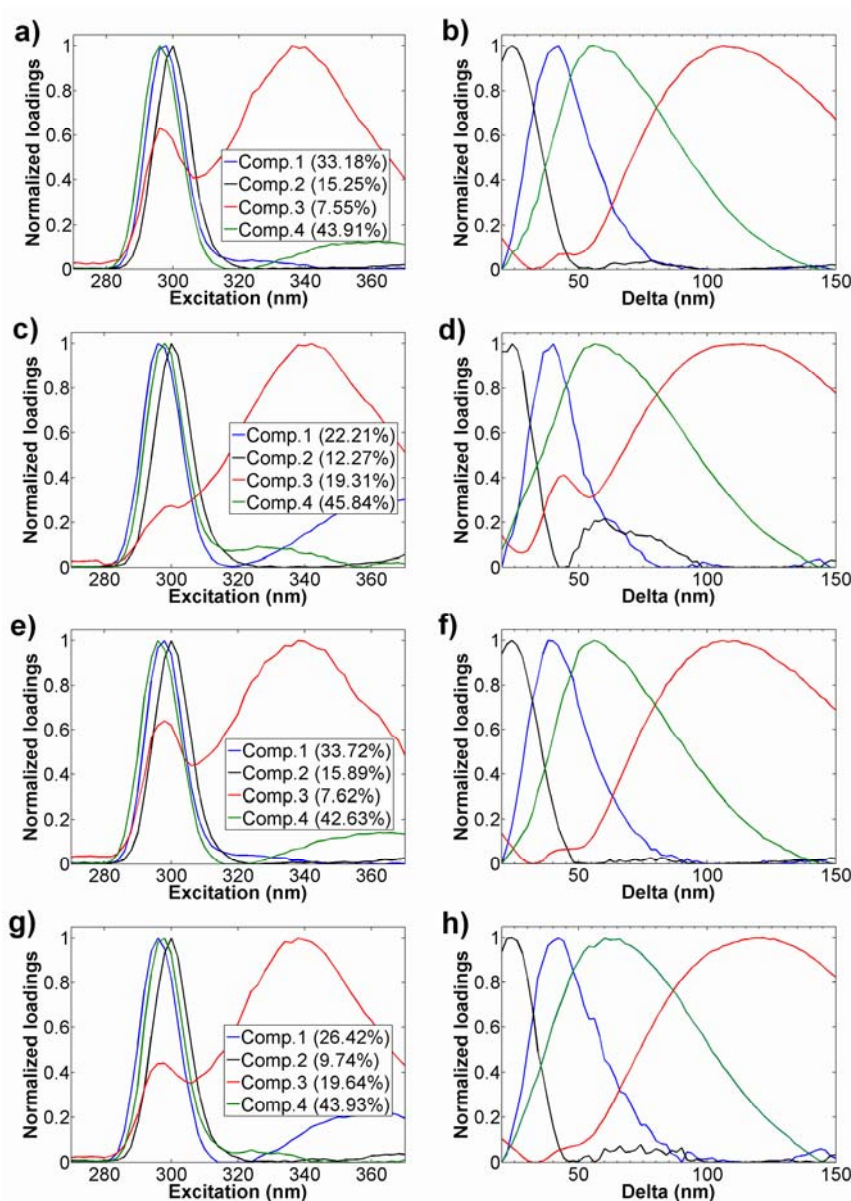

Figure 2: Normalized excitation (left) and emission, Δλ (right) profiles of the MCR model components extracted from the HH (a/b), VV (c/d), VH (e/f), and HV (g/h) polarized fluorescence datasets recorded during

.

the HSA thermal denaturation experiment. MCR analysis was performed on spectra collected over the entire temperature range, including the cooling step.

Recovered excitation profiles often appeared to have dual bands, which was an artefact caused by the TSFS data structure. Basically, RTP and amino acid emission can lie along the same $\Delta\lambda$ line but with a different λ_{ex}. This meant that MCR may not always recover a pure excitation profile and thus satellite bands were obtained. Nonetheless, it was clear which band was associated with each component. This effect can be eliminated using EEM measurements where the real excitation profiles can be extracted. However, TSFS was preferred over EEM for several reasons. First, with EEM measurements the Rayleigh scatter is an intrinsic component of the data, whereas in TSFS it is not once $\Delta\lambda > \sim 20$ nm. Rayleigh scatter is strongly polarized, thus any scattered light contamination will generate erroneous anisotropy values [1] [41]. Second, TSFS data can be collected almost twice as fast as the equivalent EEM data which is an issue considering that four TSFS spectra are required for each *aniso*-TSFS plot. Overall, for proteins the advantage of minimizing Rayleigh scatter artefacts outweighed the excitation profile recovery, however, for unknown analytes, EEM may be more advantageous. Another caveat with MCR of MDF data must be noted, the recovered excitation/emission profiles are invariant, which was a consequence of the linearity requirement for MCR [37]. This meant that the band shifts, which fluorophores experience during environmental/structural changes [1], were not explicitly extracted by MCR. This information loss about fluorophore environment was however, offset by increased quantitative information provided by the MCR scores. In summary, profiles extracted by MCR represent the best-fit spectra for each population of emitters and the scores give the relative change in contribution, which incorporates changes due to spectral shifts.
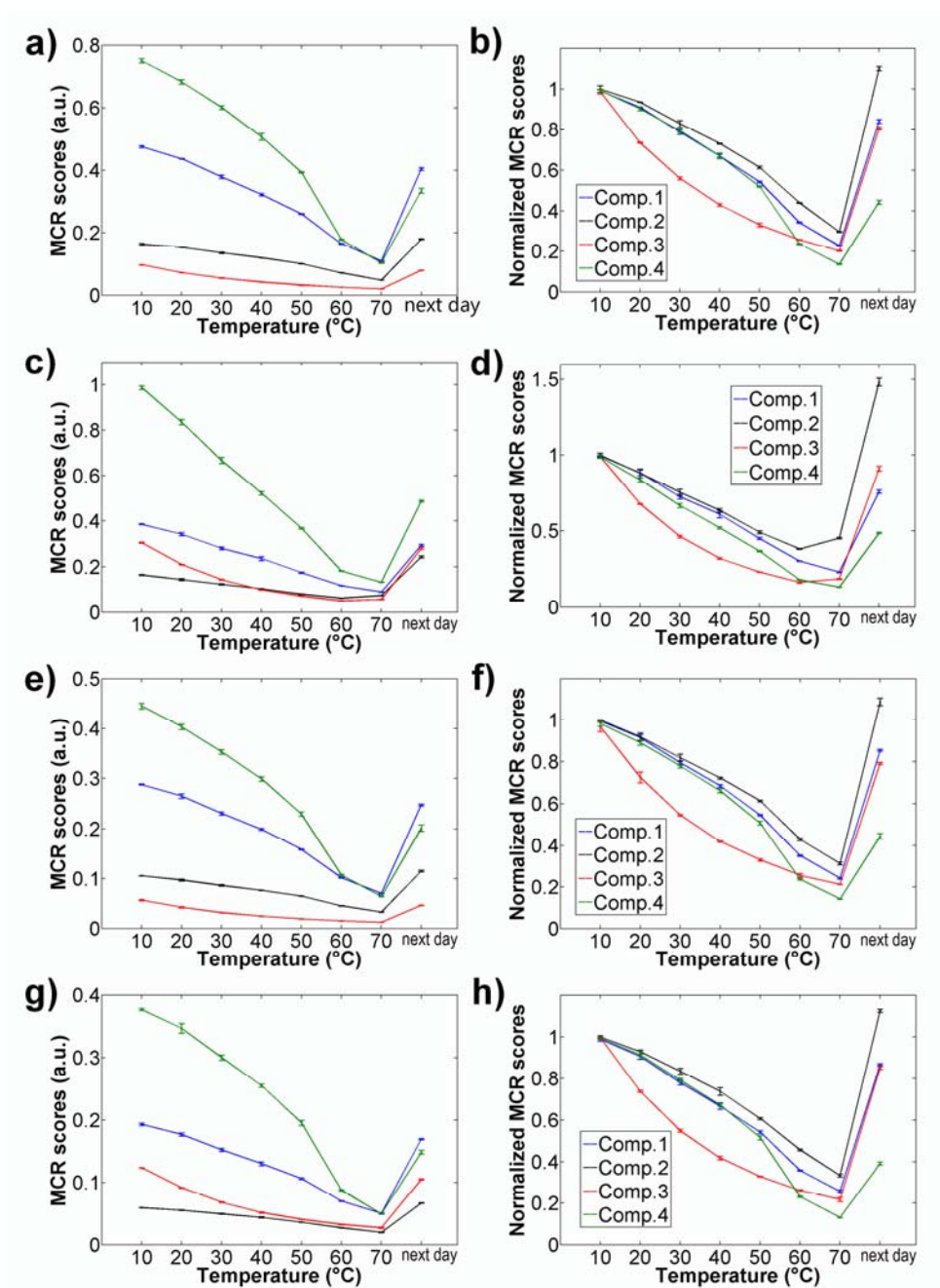
Figure 3: MCR scores plots and normalized MCR scores plots of the pure components extracted from HH (*a/b*), VV (*c/d*), VH (*e/f*), and HV (*g/h*) polarized TSFS spectra of 1 mg mL^{-1} HSA in PBS undergoing thermal unfolding from 10→70 °C and cooling from 70→20 °C. MCR score values and the error bars were calculated from the average and the standard deviations obtained from undertaking MCR separately on the replicate measurements.

All components showed higher scores (Figure 3) when the excitation and emission polarizers had the same axis of polarization (VV and HH). This was expected due to the slower fluorophore rotational speed in the more rigid protein. The normalized scores plots show that each component changed at a different rate, which indicated different fluorophore locations and processes at play. Furthermore, using the recovered pure components (Figure 2), the anisotropy at each emission wavelength for each component was then calculated (Figure

.

4). We expected that if the recovered components were real, and not composite signals caused by co-linearity in the data, that then the calculated anisotropy should be relatively constant. This was the case, apart from Comp3, where the feature at $\Delta\lambda= 45$ nm yielded an *r* value close to one, indicating that this feature was most likely scattering [1].
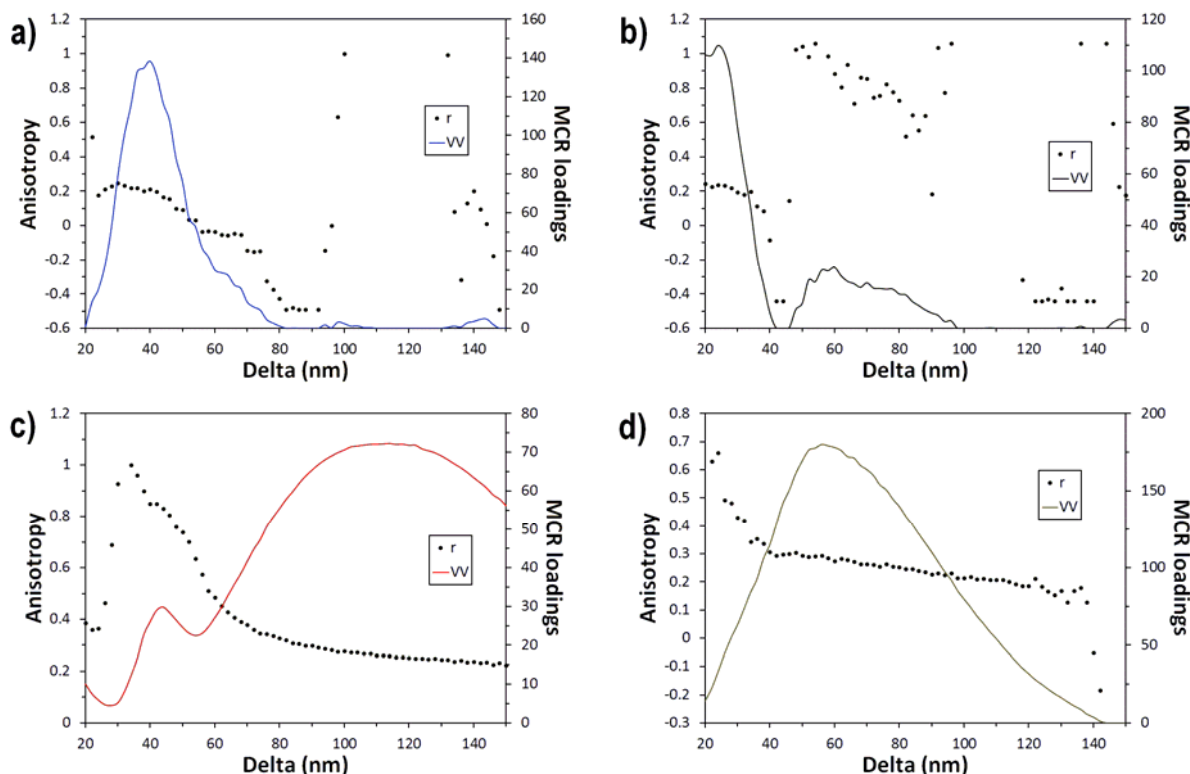

Figure 4: Wavelength dependence of anisotropy (dots) for Comp1-4 (*a-d*, respectively) with overlaid MCR generated VV emission component (continuous line). Anisotropy values >0.5 (or negative values) indicate regions of either very low spectral intensity (which lead to inaccurate *r* calculations) or scattering artefacts.

3.3 Component assignment: Component 4 (Comp4) corresponding to Trp–214 (assignment based on peak position (*SI, Fig. S-6*), high emission intensity, and literature references)[16, 18, 30] dominated emission (Figure 2) with ~42–5% of the explained variance (Table 1). Excitation profiles for Comp3 showed a weak band at ~300 nm and a strong, broad band at ~340 nm, and the corresponding emission profiles were mostly a broad band with a large $\Delta\lambda$ of ~110 nm except for the VV data, which also showed a narrow band at $\Delta\lambda$ ~45 nm. This narrow band was due to the Raman band of water as it had an anisotropy of ~1.0 and this feature was also present in TSFS spectra of PBS (*SI, Fig. S-7*). Comp3, λ_{em}~440 nm, originated from Trp RTP, and to prove this, the heavy atom method was used to increase the phosphorescence signal [5]. When MCR was re-run, Comp3 scores increased dramatically corresponding to the expected increase in RTP signal (*SI, Fig. S-8/9*). These results correlate with previously published data on HSA and other proteins, and thus confirm unambiguously the simultaneous observation/resolution of Trp phosphorescence and fluorescence.[5, 46]

.

	HH			VV			HV			VH		
Comp.	**Ex***	**Em***	**Fit (%X)** [§]	**Ex***	**Em***	**Fit (%X)** [§]	**Ex***	**Em***	**Fit (%X)** [§]	**Ex***	**Em***	**Fit (%X)** [§]
1	298	340	33.18	297	337	22.21	296	338	26.42	298	337	33.72
2	300	324	15.25	300	324	12.27	300	324	9.74	300	324	15.89
3	296, 338	444	7.55	300, 340	454	19.31	297, 338	460	19.64	298, 338	444	7.62
4	296	352	43.91	298	354	45.84	298	358	43.93	296	352	42.63

* Ex and Em represent the peak maxima in the recovered excitation and emission profiles from the MCR model. $\Delta\lambda$ represents the difference between λ_{em} and λ_{ex}, and the maximum emission wavelengths were calculated accordingly).

[§] Fit %X is the %var captured by each MCR model component (the sum-squared signal relative to the total signal in the data.

Table 1: Summary of the components extracted by the MCR models obtained for the four differently polarized TSFS datasets collected from HSA (1 mg mL^{-1} PBS buffer) that had been thermally stressed. Each dataset contained samples measured between 10 and 70 °C, and the post-stressed cooled sample.

Comp1 and Comp2 have emission maxima of 337–340 nm and 324 nm, respectively, arising from *two* different emitting tyrosine populations. Comp1 represented the combined emissions of tyrosines located in the more solvent exposed subdomain IIA/B (Tyr-263/-319/-332/-334/-341/-353/-367) which are all relatively close to Trp-214 and thus more sensitive to FRET (R_0 for Trp-Tyr varies from 9 to 18 Å depending on quantum yield and other factors) [1]. Comp2 represented the combined emission of all the other 11 Tyr residues: four located in the more hydrophobic subdomain IIIA (Tyr-401/-411/-452/-497), five located in subdomain IB (Tyr-138/-140/-148/-150/-161), and two in IA (Tyr-30/-84) [47], which accounted for the emission blue shift. Most of this second population were all further away (>15 Å) from Trp-214 (*Supplementary, Fig. S-1*) and should be slightly less FRET sensitive. However, Comp2 shows a weak secondary band at an emission wavelength corresponding to Trp, and we surmise that this may be due to Tyr-Trp FRET involving Tyr-452 (in domain IIIA) which is relatively close. However, anisotropy values calculated in this region are unreliable because the measured intensity of the raw data was too low in 3 out of 4 cases (Figure 2) [41]. The FRET-anisotropy issue here is very complex because four competing factors are at play: physical separation between the fluorophores and chromophores, emission wavelength, quantum yield, and lifetime, all of which influence FRET and therefore anisotropy.

	HH			VV			HV			VH		
Comp.	**Ex***	**Em***	**Fit (%X)§**	**Ex**	**Em**	**Fit (%X)§**	**Ex**	**Em**	**Fit (%X)§**	**Ex**	**Em**	**Fit (%X)§**
1b	298	340	38.4	297	337	17.7	296	338	25.52	298	337	30.8
1a	298	340	32.9	298	338	13.2	296	338	21.12	297	338	31.7
2b	300	324	14.4	300	324	9.6	300	324	8.98	300	324	14.3
2a	300	326	15.6	300	326	8.8	300	326	8.65	300	326	16.1
3b	296, 338	**444**	**7.4**	300, 340	**454**	**21.9**	297, 338	**460**	**18.87**	298, 338	**444**	**7.6**
3a	298, 340	**448**	**15.4**	342	**460**	**43.1**	298, 338	**460**	**34.93**	298, 338	**446**	**15.7**
4b	296	352	39.6	298	354	50.5	298	358	46.42	296	352	47.2
4a	296	350	35.9	296	348	34.4	296	352	34.76	296	350	36.2

* Ex and Em represent the peak maxima in the recovered excitation and emission profiles from the MCR model. $\Delta\lambda$ represents the difference between λ_{em} and λ_{ex}, and the maximum emission wavelengths were calculated accordingly).

§ Fit %X is the %var captured by each MCR model component (the sum-squared signal relative to the total signal in the data.

Table 2: Comparison of the MCR models generated before (b) and after (a) addition of Na_2SO_3/KI to HSA solutions (1 mg mL^{-1} in PBS buffer). These MCR models used only sample data collected over a 10–30 °C temperature range.

The variation captured by Comp2 was significantly lower than for Comp1 which was a consequence of the emission profile of Comp2 being incomplete as the emission maximum appears close to the lower $\Delta\lambda$ range limit. The Tyr assignments agreed with the RTP study results where we saw a decrease in the contribution from Comp1 (Table 2) as the triplet pathway for Trp emission was facilitated, indicating an interlinked FRET pathway with this Tyr population. The other Tyr population being further away was not affected significantly. The fluorophore assignments and spectral data from the extracted components all agreed with previously published data [46]. To validate MCR Trp/Tyr band assignment, ARMES data was collected from mixtures of Trp and Tyr in glycerol (*SI, Fig. S-10*). MCR analysis showed three components, one for Tyr, one for Trp, and the RTP with similar profiles to those recovered from HSA.

3.4 Monitoring thermal denaturation by ARMES: Comp3 (RTP) showed a consistent rate of decrease down to 70 °C (Figure 3) indicating that thermal quenching of RTP was occurring. When Comp3 MCR scores data from the RTP experiment were normalized we got the same trend and the plot of ln(MCR scores) *versus* 1/T gave straight-line plots (*SI, Fig. S-11*). This clearly indicated an Arrhenius like process, in other words a bimolecular quenching of RTP. Comp 4 (Trp fluorescence) showed a clear multi-step process in all datasets, with a gradual decrease of MCR scores up to ~40/50 °C, followed by a steep drop between~50–60 °C as the HSA unfolds, exposing Trp-214 to a polar environment. From 60–70 °C there was then again a small decrease. This agreed with the three-step model with the expanded form being generated up to ~40 °C, the second step between 50–60 °C with the unfolding of domain II,

.

followed by complete, irreversible unfolding at temperatures above ~60 °C [17, 18, 48-50]. Comp1/2 displayed similar yet non-identical changes in normalized MCR scores, signifying the different locations of the Tyr residues contributing to each signal. Comp1 (Tyr in subdomain IIB) scores changes were closer in profile to Comp4, which may be due to the closeness of the IIA and IIB subdomains, and the resulting change in FRET efficiencies. Tyr residues located in the more hydrophobic IA/IB/IIIA domains (Comp2) show the least dramatic changes, and weakest intensities because of their relatively low quantum yields.
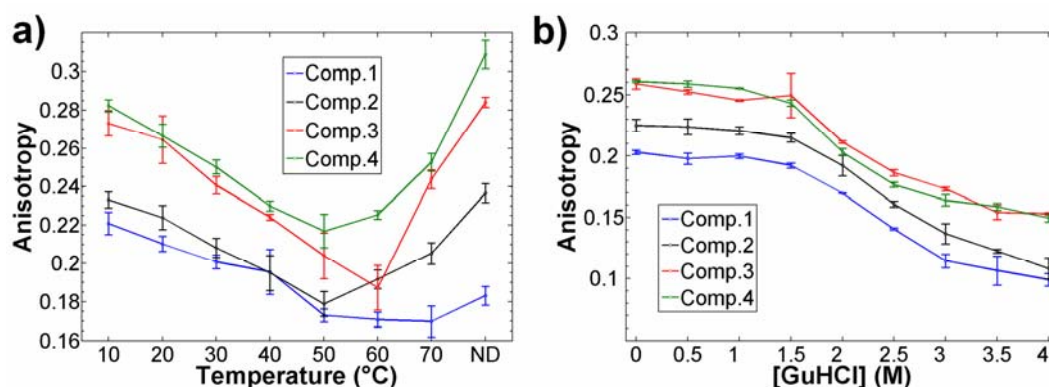
Figure 5: Plot of the anisotropy change for each component obtained from the MCR models of 1 mg mL^{-1} HSA in PBS: **(a)** with increase in temperature and cooling overnight from 70→20 °C (ND), and **(b)** with increasing GuHCl concentration. Anisotropy was calculated for the wavelength of maximum intensity of each reconstructed component. The average of three values was plotted, with the standard deviation as the error bar.

Another view of the unfolding processes was obtained by evaluating the anisotropy plots of each component (Figure 5). For RTP (Comp3), anisotropy decreased almost linearly indicating that the observation was a thermal quenching of phosphorescence and that the RTP signal was seemingly independent of the thermally induced structural changes. The Comp3 anisotropy value calculated for 70 °C was almost certainly unreliable, as the measured phosphorescence intensity (as measured by MCR scores) did not agree. This outlier was caused by the very low emission intensity (<5%) recorded for the VV data (Figure 3).

For Comp4 (Trp, subdomain IIA) a linear decrease was observed from 10–40 °C, then a slight decrease in slope between 40–50 °C, followed by an increased anisotropy for 60/70 °C as the protein unfolds. The anisotropy values recovered here at 20 °C were much higher than those reported by other groups such as Flora *et al.*[17] (0.27 *versus* 0.18). This was because ARMES recovered only Trp fluorescence, which ensured minimal contribution from RTP or Tyr emission to the anisotropy measurement. At 20 °C, HSA contains ~65-6% α-helix content, which decreased to ~ 53% at 65 °C as denaturation progresses [18, 49]. The anisotropy drop (Figure 5a) corresponds to loss in rigidity caused by the loss in α-helicity for each subdomain. Above 50 °C, the measured anisotropy increase for Comp2/4 could reflect increased β-structure formation because HSA at 25 °C was reported to have a 5-7% β-sheet content, while long-term exposure at 65 °C gives a ~20% β-content [51, 52]. This is probable since analysis of recombinant domains of HSA indicate that domain II has a relatively high β-sheet content of ~34% at 25 °C.

.

The contrast between chemical and thermal denaturation in terms of component anisotropy (Figure 5a/b) was striking. Measureable changes in protein structure start to occur at GuHCl concentrations of 1–1.5M and with a maximum unfolding at 4M GuHCl where a highly random coil conformation was obtained. Anisotropy plots for each component showed clearly that this was a single step transition between the native and the unfolded states, because the anisotropy change was the same for each emitter. This agreed with previously published results [53, 54], for example, initial (0M)/final (4M) anisotropy ratios (~1.7) for both Trp components were close the mean lifetime ratio (1.9) from Flora *et al*.[17] Comparing the MCR scores (Figure 3, and *SI, Fig. S-12/13*) shows very different behavior and it was interesting to note that the Comp3 (RTP) contribution increased in a sigmoidal fashion (centered at 2M GuHCl) as GuHCl concentration increased. This comparison showed unambiguously how fundamentally different the denaturation methods are in terms of effect on intrinsic emission and how ARMES provides another layer of information for structural change elucidation.

3.5 Refolded structure analysis: After thermal denaturation, HSA solutions were cooled overnight to 20 °C and *aniso*-TSFS data recollected. Neither anisotropy (Figure 5) nor MCR scores (Figure 3) returned to starting values thus proving that the refolded structure after thermal denaturation was different. For example, Comp4 anisotropy (Trp-214) at 20 °C changed from 0.27 in the native state to r=0.31 on refolding after cooling from 70 °C. This was clear proof that refolding of the hydrophobic pocket in subdomain IIA resulted in *either* a more rigid structure where the local motion of the Trp was restricted compared to native state, or, that the refolded state was more solvent exposed, leading to a Trp lifetime reduction which would account for an increased anisotropy. Here, the second option was more probable, as reports have shown that there was a decreased Trp lifetime for HSA denaturation due to increased solvent exposure after recovery from thermal denaturation. The increased anisotropy was ~11% which was the same as the mean lifetime decrease of 5.28 to 4.72 ns recorded by Flora *et al*. [17]. This was supported by evaluation of MCR scores (Figure 3) where Comp4 scores were always much less after refolding which indicated higher quenching due to solvent exposure. To understand more about the refolded subdomain IIA state we considered the RTP signal where a slightly higher anisotropy was obtained, which again could be caused by two factors: a change in local rigidity or fluorophore lifetime. However, MCR showed that Comp3 was always greater after refolding indicative of a more restricted environment. This combination of fluorescence and RTP data clearly proves that subdomain IIA, became more rigid, but solvent exposed in the refolded HSA after thermal denaturation above 60 °C. This agreed with Mitra's conclusions from time-resolved and hydration studies that subdomain IIA native structure was not fully recovered upon cooling [18].

For the Tyr based components, anisotropy recovery on refolding differed. Comp1 recovered to 0.18 (80%) indicating that subdomain IIB did not recover fully to the native state. This agreed with observations that after cooling, the protein recovered to only ~50% α-helicity as subdomain IIB remains unfolded [18, 49]. Comp2 on the other hand recovered to a higher anisotropy of ~ 0.24, indicating that hydrophobic subdomain IIIA refolded into a similar, but more compact structure compared to the native state. This can be explained by

.

the fact that unfolding of subdomain IIIA exposed a smaller hydrophobic area to the solvent compared to the unfolding of subdomain IIA, which leads to lower structural disruption [15, 55]. This behavior was obvious from the scores plots where the degree of change in Comp1 was greater than that for Comp2.

4. Conclusions

ARMES can be defined as the resolving of fluorophore emission from mixtures based on the differential emission polarization of the constituent fluorophores caused by variations in rotational correlation times or fluorescence lifetimes, which is achieved by the use of multi-way chemometrics. The ARMES method in this iteration with its combined use of *aniso*-TSFS and MCR based analysis provides a unique approach for studying protein unfolding/folding/denaturation processes. Since anisotropy in multi-fluorophore macromolecules was fundamentally sensitive to both emission and excitation wavelengths we get unique spectral data, which can be analyzed using MCR to show how the emission of each fluorophore (or groups of closely related fluorophores) changes in terms of both intensity and anisotropy. The anisotropy element in particular facilitates the resolution of near identical fluorophores, which have overlapping emission spectra. ARMES can be considered as being analogous to time-resolved emission spectroscopy (TRES). However, it does not require the use of complicated time-resolved instrumentation, and furthermore it can resolve overlapping fluorophores that have very similar lifetimes based on their local rigidity.

For HSA in solution, ARMES recovered four emitting species, three fluorescent and one phosphorescent. This resolving of RTP from the stronger overlapping fluorescence was a key advantage of this method. Furthermore, by following the MCR scores of the raw data and the *aniso*-TSFS data we were able to easily follow the unfolding process and unambiguously identify different processes, and changes in refolded HSA. Even with the limitations of MCR recovered emission/excitation spectra, the method provides a unique tool, which can be used for *an*y multi-fluorophore macromolecular system in its present form.

As with many fluorescence techniques ARMES is non-destructive and relatively rapid, but has distinct advantages in uses standard fluorescence spectrophotometers, requires no extrinsic labels, and delivers a wealth of information simultaneously about all the fluorophores. Another big advantage if the fact that it is also feasible to recover ARMES data from samples in which there is interfering background signals from small molecule fluorophores, enabling *in-situ* protein characterization, for example in the presence of cell culture media [41]. The current limitations of the method as currently implemented are largely related to the time taken to collect all four constituent HH, VV, HV, and VH measurements and time required for data analysis. This limits its application for kinetic measurements, and reduces the scope for high throughput screening applications. However, these limitations might be overcome through revised spectrometer design and the automation of the data analysis methods.

5. Supplemental information available

Supporting information is available and includes further details on the spectral and quantitative analyses.

References:

[1]   J.R. Lakowicz, Principles of Fluorescence Spectroscopy, Springer, New York, 2006.

[2]   I.B. Bekard, D.E. Dunstan, Tyrosine Autofluorescence as a Measure of Bovine Insulin Fibrillation, Biophys. J., 97 (2009) 2521-2531.

[3]   D.M. Togashi, A.G. Ryder, D. O'Shaughnessy, Monitoring local unfolding of bovine serum albumin during denaturation using steady-state and time-resolved fluorescence spectroscopy, Journal of Fluorescence, 20 (2010) 441-452.

[4]   E. Lissi, C. Calderon, A. Campos, Evaluation of the Number of Binding Sites in Proteins from their Intrinsic Fluorescence: Limitations and Pitfalls, Photochem. Photobiol., 89 (2013) 1413-1416.

[5]   K. Sagoo, R. Hirsch, P. Johnston, D. McLoskey, G. Hungerford, Pre-denaturing transitions in human serum albumin probed time-resolved phosphorescence using, Spectroc. Acta Pt. A-Molec. Biomolec. Spectr., 124 (2014) 611-617.

[6]   M.M. Khan, S. Muzammil, S. Tayyab, Role of salt bridge(s) in the binding and photoconversion of bilirubin bound to high affinity site on human serum albumin, Biochim. Biophys. Acta-Protein Struct. Molec. Enzym., 1479 (2000) 103-113.

[7]   J.K. Armstrong, R.B. Wenby, H.J. Meiselman, T.C. Fisher, The hydrodynamic radii of macromolecules and their effect on red blood cell aggregation, Biophys. J., 87 (2004) 4259-4270.

[8]   N. Sattarahmady, A.A. Moosavi-Movahedi, F. Ahmad, G.H. Hakimelahi, M. Habibi-Rezaei, A.A. Saboury, N. Sheibani, Formation of the molten globule-like state during prolonged glycation of human serum albumin, Biochim. Biophys. Acta-Gen. Subj., 1770 (2007) 933-942.

[9]   R. Yadav, B. Sengupta, P. Sen, Conformational Fluctuation Dynamics of Domain I of Human Serum Albumin in the Course of Chemically and Thermally Induced Unfolding Using Fluorescence Correlation Spectroscopy, J. Phys. Chem. B, 118 (2014) 5428-5438.

[10]   U. Kragh-Hansen, V.T.G. Chuang, M. Otagiri, Practical aspects of the ligand-binding and enzymatic properties of human serum albumin, Biol. Pharm. Bull., 25 (2002) 695-704.

[11]   J. Ghuman, P.A. Zunszain, I. Petitpas, A.A. Bhattacharya, M. Otagiri, S. Curry, Structural basis of the drug-binding specificity of human serum albumin, J. Mol. Biol., 353 (2005) 38-52.

[12]   F. Kratz, Albumin as a drug carrier: Design of prodrugs, drug conjugates and nanoparticles, Journal of Controlled Release, 132 (2008) 171-183.

[13]   S. Curry, H. Mandelkow, P. Brick, N. Franks, Crystal structure of human serum albumin complexed with fatty acid reveals an asymmetric distribution of binding sites, Nat. Struct. Biol., 5 (1998) 827-835.

[14]   S. Sugio, A. Kashima, S. Mochizuki, M. Noda, K. Kobayashi, Crystal structure of human serum albumin at 2.5 angstrom resolution, Protein Eng., 12 (1999) 439-446.

[15]   M.K. Santra, A. Banerjee, O. Rahaman, D. Panda, Unfolding pathways of human serum albumin: Evidence for sequential unfolding and folding of its three domains, International Journal of Biological Macromolecules, 37 (2005) 200-204.

[16]   O.K. Abou-Zied, O.I.K. Al-Shihi, Characterization of subdomain IIA binding site of human serum albumin in its native, unfolded, and refolded states using small molecular probes, J. Am. Chem. Soc., 130 (2008) 10793-10801.

.

[17]   K. Flora, J.D. Brennan, G.A. Baker, M.A. Doody, F.V. Bright, Unfolding of acrylodan-labeled human serum albumin probed by steady-state and time-resolved fluorescence methods, Biophys. J., 75 (1998) 1084-1096.

[18]   R.K. Mitra, S.S. Sinha, S.K. Pal, Hydration in protein folding: Thermal unfolding/refolding of human serum albumin, Langmuir, 23 (2007) 10224-10229.

[19]   I.M. Vlasova, A.M. Saletsky, Study of the Denaturation of Human Serum Albumin by Sodium Dodecyl Sulfate Using the Intrinsic Fluorescence of Albumin, Journal of Applied Spectroscopy, 76 (2009) 536-541.

[20]   G.A. Pico, Thermodynamic features of the thermal unfolding of human serum albumin, International Journal of Biological Macromolecules, 20 (1997) 63-73.

[21]   R. Wetzel, M. Becker, J. Behlke, H. Billwitz, S. BöHm, B. Ebert, H. Hamann, J. Krumbiegel, G. Lassmann, Temperature Behaviour of Human Serum Albumin, European Journal of Biochemistry, 104 (1980) 469-478.

[22]   I.M. Warner, G.D. Christian, E.R. Davidson, J.B. Callis, Analysis of Multicomponent Fluorescence Data, Anal. Chem., 49 (1977) 564-573.

[23]   D. Patra, A.K. Mishra, Recent developments in multi-component synchronous fluorescence scan analysis, Trac-Trends Anal. Chem., 21 (2002) 787-798.

[24]   P.W. Ryan, B. Li, M. Shanahan, K.J. Leister, A.G. Ryder, Prediction of Cell Culture Media Performance Using Fluorescence Spectroscopy, Anal. Chem., 82 (2010) 1311-1317.

[25]   J. Bridgeman, M. Bieroza, A. Baker, The application of fluorescence spectroscopy to organic matter characterisation in drinking water treatment, Rev. Environ. Sci. Bio-Technol., 10 (2011) 277-290.

[26]   B. Li, P.W. Ryan, M. Shanahan, K.J. Leister, A.G. Ryder, Fluorescence EEM Spectroscopy for Rapid Identification and Quality Evaluation of Cell Culture Media Components., Appl. Spectrosc., 65 (2011) 1240-1249.

[27]   A. Calvet, B. Li, A.G. Ryder, A rapid fluorescence based method for the quantitative analysis of cell culture media photo-degradation, Anal. Chim. Acta, 807 (2014) 111-119.

[28]   B. Li, M. Shanahan, A. Calvet, K.J. Leister, A.G. Ryder, Comprehensive, quantitative bioprocess productivity monitoring using fluorescence EEM spectroscopy and chemometrics, Analyst, 139 (2014) 1661-1671.

[29]   E.A. Burstein, N.S. Vedenkin, M.N. Ivkova, Fluorescence and the Location of Tryptophan Residues in Protein Molecules, Photochem. Photobiol., 18 (1973) 263-279.

[30]   N. Tayeh, T. Rungassamy, J.R. Albani, Fluorescence spectral resolution of tryptophan residues in bovine and human serum albumins, J. Pharm. Biomed. Anal., 50 (2009) 107-116.

[31]   K.R. Grigoryan, Fluorescent Analysis of the Structural Changes of Human Serum Albumin Induced by Low Temperatures in Water-Dimethyl Sulfoxide Solutions, Russ. J. Phys. Chem. A, 85 (2011) 317-320.

[32]   K.R. Grigoryan, H.A. Shilajyan, Intermolecular interactions in albumin-sulfoxide-water systems at low temperatures, investigated by means of fluorescence quenching, Russ. J. Phys. Chem. A, 87 (2013) 780-782.

[33]   J.M. Amigo, F. Marini, in: M. Federico (Ed.), Data Handling in Science and Technology, Elsevier, 2013, p. 265-313.

[34]   J.H. Jiang, Y. Ozaki, Self-modeling curve resolution (SMCR): Principles, techniques, and applications, Applied Spectroscopy Reviews, 37 (2002) 321-345.

[35]   M.C.G. Antunes, J. da Silva, Multivariate curve resolution analysis excitation-emission matrices of fluorescence of humic substances, Anal. Chim. Acta, 546 (2005) 52-59.

.

[36]   J.C.G.E. da Silva, R. Tauler, Multivariate curve resolution of synchronous fluorescence spectra matrices of fulvic acids obtained as a function of pH, Appl. Spectrosc., 60 (2006) 1315-1321.

[37]   A. de Juan, R. Tauler, Multivariate curve resolution (MCR) from 2000: Progress in concepts and applications, Crit. Rev. Anal. Chem., 36 (2006) 163-176.

[38]   R. Bro, PARAFAC. Tutorial and applications, Chemometr. Intell. Lab. Syst., 38 (1997) 149-171.

[39]   C. Andersen, R. Bro, Practical aspects of PARAFAC modeling of fluorescence excitation-emission data, J. Chemometr., 17 (2003) 200-215.

[40]   H. Chen, J.E. Kenny, Application of PARAFAC to a two-component system exhibiting Fluorescence Resonance Energy Transfer: from theoretical prediction to experimental validation, Analyst, 137 (2012) 153-162.

[41]   R.C. Groza, A. Calvet, A.G. Ryder, A fluorescence anisotropy method for measuring protein concentration in complex cell culture media, Anal Chim Acta, 821 (2014) 54-61.

[42]   Y.J. Liu, H.L. Wu, C. Kang, H.W. Gu, J.F. Nie, S.S. Li, Z.Y. Su, R.Q. Yu, Four-way Self-weighted Alternating Normalized Residue Fitting Algorithm with Application for the Analysis of Serotonin in Human Plasma, Analytical Sciences, 28 (2012) 1097-1104.

[43]   A.C. Olivieri, J.A. Arancibia, A.M. de la Pena, I. Duran-Meras, A.E. Mansilla, Second-order advantage achieved with four-way fluorescence excitation-emission-kinetic data processed by parallel factor analysis and trilinear least-squares. Determination of methotrexate and leucovorin in human urine, Anal. Chem., 76 (2004) 5657-5666.

[44]   C.J. Xu, Y.Z. Liang, Y. Li, Y.P. Du, Chemical rank estimation by noise perturbation in functional principal component analysis, Analyst, 128 (2003) 75-81.

[45]   Y. Hu, B.Y. Li, H. Sato, I. Noda, Y. Ozaki, Noise perturbation in functional principal component analysis filtering for two-dimensional correlation spectroscopy: Its theory and application to infrared spectra of a poly(3-hydroxybutyrate) thin film, Journal of Physical Chemistry A, 110 (2006) 11279-11290.

[46]   Y. Wei, C. Dong, D. Liu, S. Shuang, C.W. Huie, Enantioselective quenching of room-temperature phosphorescence lifetimes of proteins: bovine and human serum albumins, Biomacromolecules, 8 (2007) 761-764.

[47]   S. Tabassum, W.M. Al-Asbahy, M. Afzal, F. Arjmand, R.H. Khan, Interaction and photo-induced cleavage studies of a copper based chemotherapeutic drug with human serum albumin: spectroscopic and molecular docking study, Molecular bioSystems, 8 (2012) 2424-2433.

[48]   Y. Moriyama, K. Takeda, Re-formation of the helical structure of human serum albumin by the addition of small amounts of sodium dodecyl sulfate after the disruption of the structure by urea. A comparison with bovine serum albumin, Langmuir, 15 (1999) 2003-2008.

[49]   Y. Moriyama, K. Takeda, Protective effects of small amounts of bis(2-ethylhexyl)sulfosuccinate on the helical structures of human and bovine serum albumins in their thermal denaturations, Langmuir, 21 (2005) 5524-5528.

[50]   M. Rezaei-Tavirani, S.H. Moghaddamnia, B. Ranjbar, M. Amani, S.A. Marashi, Conformational study of human serum albumin in pre-denaturation temperatures by differential scanning calorimetry, circular dichroism and UV spectroscopy, J. Biochem. Mol. Biol., 39 (2006) 530-536.

[51]   M. Dockal, D.C. Carter, F. Ruker, Conformational transitions of the three recombinant domains of human serum albumin depending on pH, Journal of Biological Chemistry, 275 (2000) 3042-3050.

[52]   J. Juarez, P. Taboada, V. Mosquera, Existence of Different Structural Intermediates on the Fibrillation Pathway of Human Serum Albumin, Biophys. J., 96 (2009) 2353-2370.

.

[53]   S.S. Krishnakumar, D. Panda, Spatial relationship between the prodan site, Trp-214, and Cys-34 residues in human serum albumin and loss of structure through incremental unfolding, Biochemistry, 41 (2002) 7443-7452.

[54]   S. Muzammil, Y. Kumar, S. Tayyab, Anion-induced stabilization of human serum albumin prevents the formation of intermediate during urea denaturation, Proteins, 40 (2000) 29-38.

[55]   B. Farruggia, F. Rodriguez, R. Rigatuso, G. Fidelio, G. Pico, The participation of human serum albumin domains in chemical and thermal unfolding, J. Protein Chem., 20 (2001) 81-89.

SUPPLEMENTARY INFORMATION:
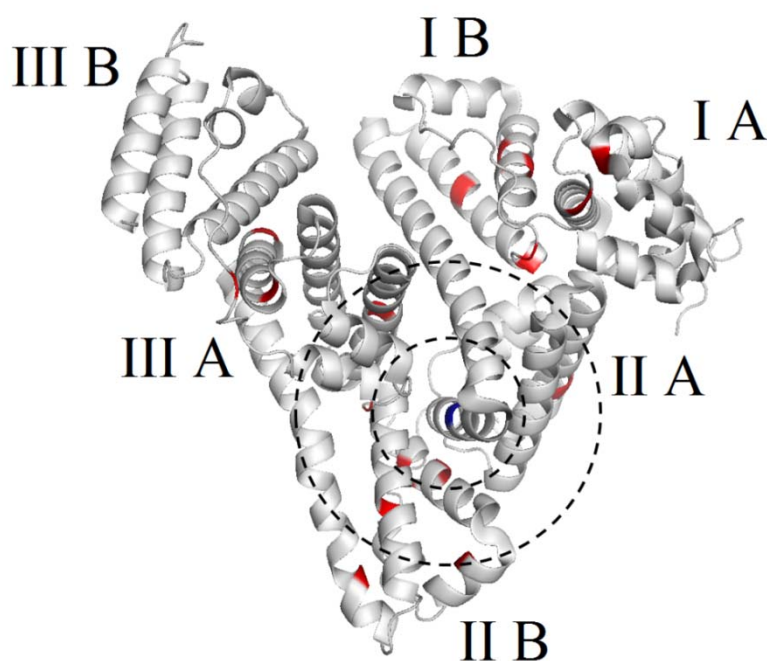
Figure S-6: HSA structure showing Tyrosine (red) and Tryptophan (blue) locations. The dashed circles represent the minimum and maximum Förster radius for the Trp-Tyr pair (9-18 Å) as reported in Lakowicz.[1]

.
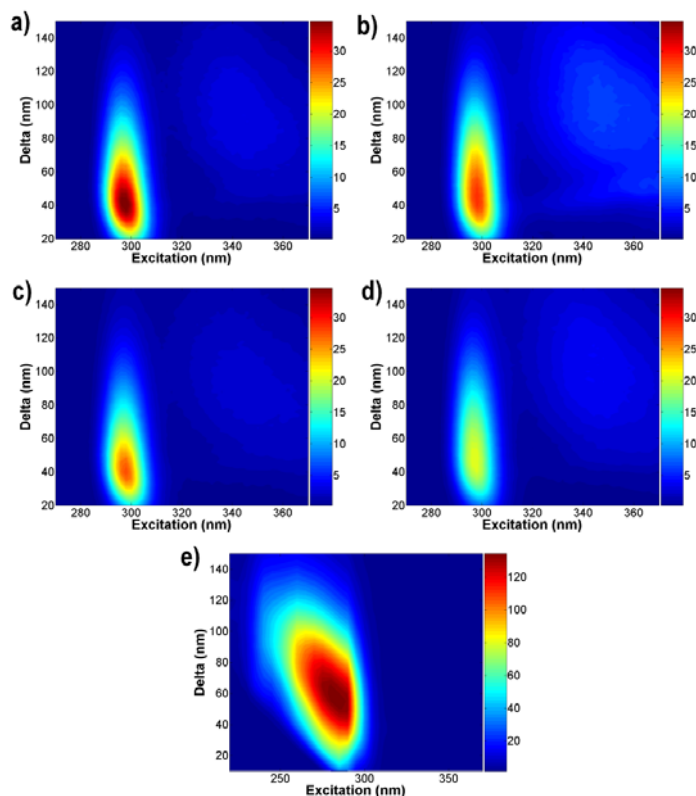
Figure S-7: TSFS spectra of HSA (1 mg mL^{-1}) in PBS at 20ºC: *a)* HH, *b)* VV, *c)* VH, *d)* HV polarized, and *e)* Standard (non-polarized)TSFS spectrum.

Note: Polarizer filters & effect on excitation spectra.

The polarizers used in the Cary Eclipse are polymer based thin film based and have a spectral cut-off at ~290 nm (*see Figure S-3*). Below this most of (>99%) the excitation light is absorbed by the filter material and thus there is no excitation. Likewise, in the emission pathway, filter absorption starts to become significant below ~300 nm.

.
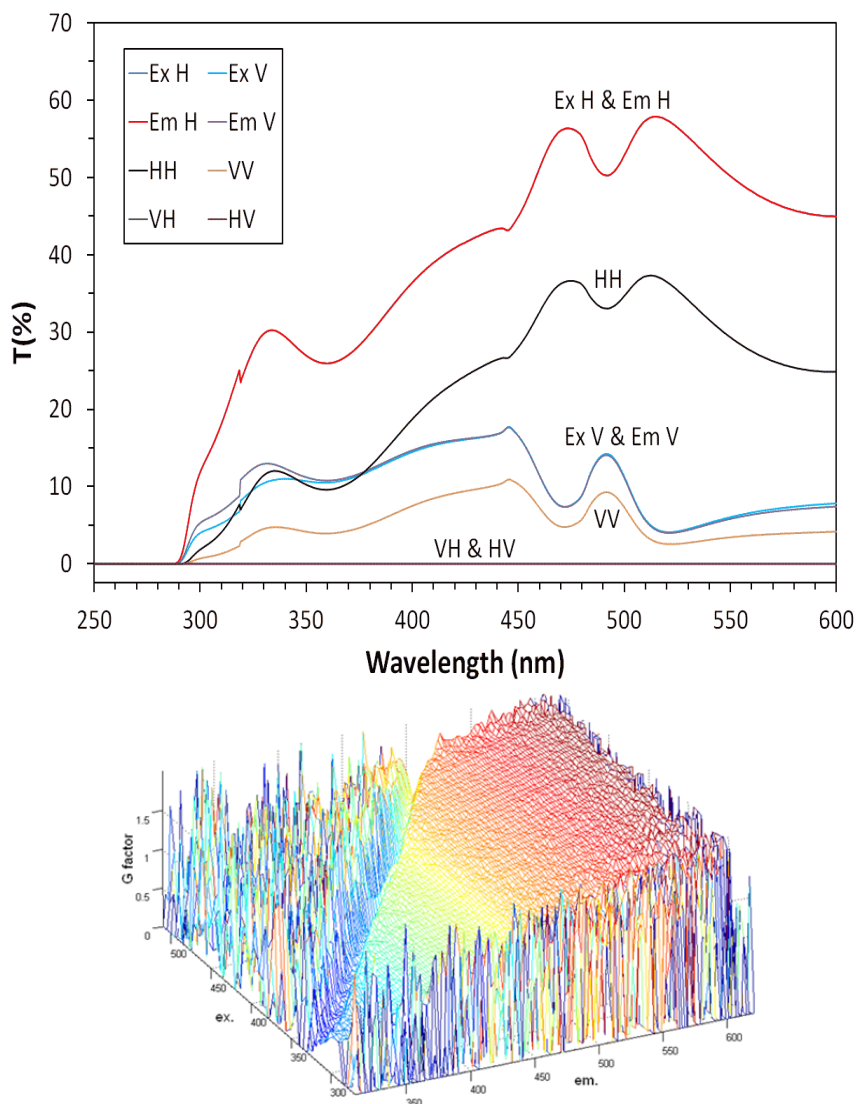
Figure S-8: (Top) Transmittance spectra of the excitation and emission polarizer filters oriented individually in vertical and horizontal positions, and as crossed, aligned combinations. Spectra recorded using a Shimadzu UV-1601 spectrometer with a 0.2 nm sampling interval. The centre of the polarizer was aligned normal to the light beam. The discontinuity at ~320 nm is due to light source switch over in the spectrometer and is not a feature of the polarizers. **(Bottom)** Emission-excitation landscape plot of the calculated G-factor for the detection system. The areas of high noise were typically excluded because they had fluorescence intensities below the 10% threshold.

Most standard fluorescence spectrometers use these thin film polarizers as standard for anisotropy measurements.   The UV usable range for anisotropy measurements can be extended via the use of UV transmitting wire grid polarizers.   However, this was not an option that could be implemented for this study (or is commonly offered as an option in laboratory-based systems).

.
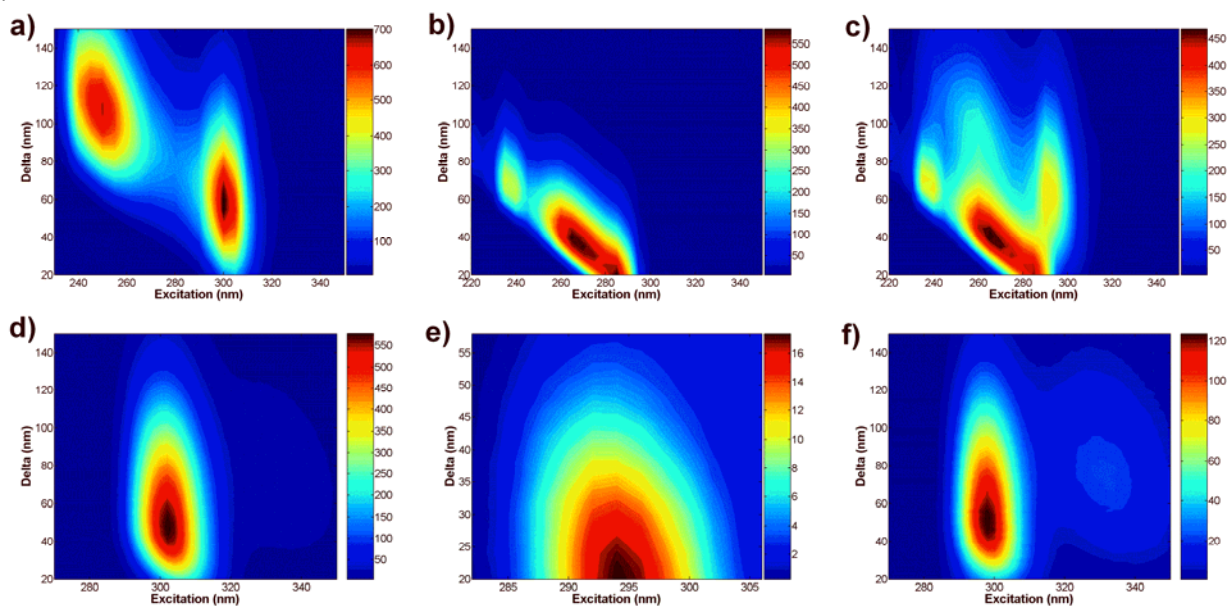
Figure S-9: Normal TSFS (top) and HH polarised TSFS (middle) plots for: (left column) N-acetyl-tryptophan (10^{-3} M), (middle column) N-acetyl-tyrosine (10^{-3} M), and (right column) a mixture (18:1 molar ratio of N-acetyl-Tyr and N-acetyl-Trp, 10^{-3} M total concentration) in 90% glycerol.
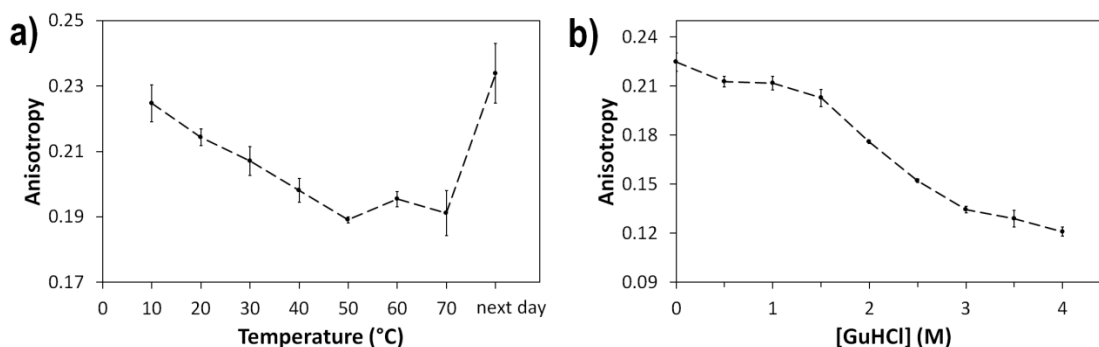

Figure S-5: Changes in average anisotropy for HSA (1mg mL^{-1}) for *a)* thermal denaturation (10–70°C and cooling to 20ºC), and *b)* chemical denaturation using GuHCl (0–4 M) at 25°C. The average anisotropy was calculated by taking the average of all points measured over the λ_{ex} = 290–305nm and $\Delta\lambda$ = 40nm (*e.g.* λ_{em} = 330–345nm) spectral range.

.
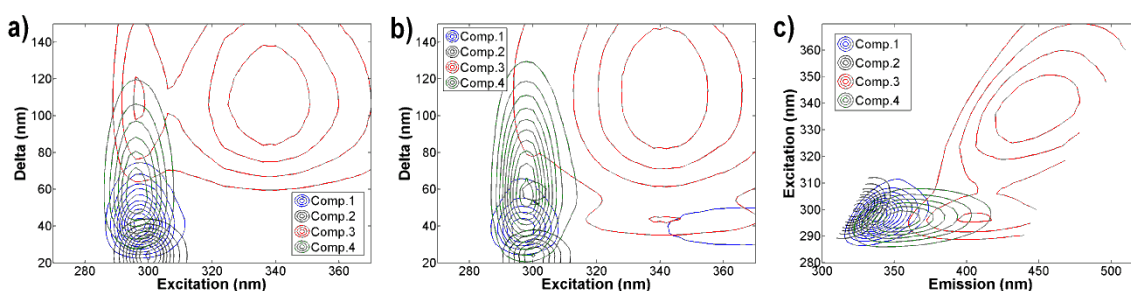
Figure S-6: Landscape plots showing the reconstructed pure MCR components for *a)* HH polarized TSFS, *b)* VV polarized TSFS, and *c)* HH polarized EEM generated from the TSFS data. For components, 1, 2, and 4 the contour lines have the same separation. For component 3, the contour line separation is much less because of the weakness of the signal.
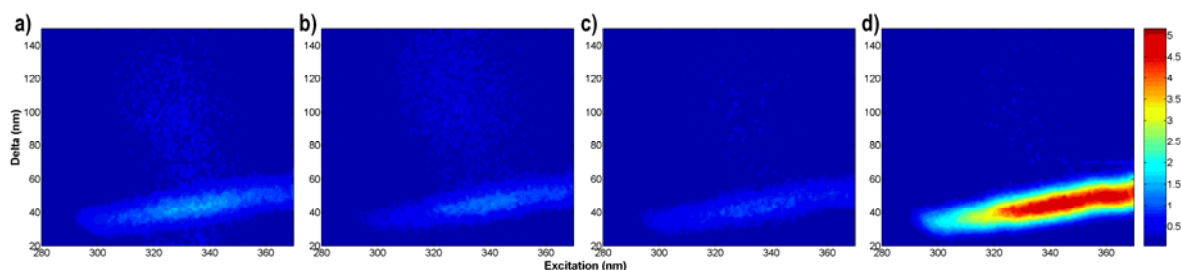

Figure S-7: TSFS spectra of PBS buffer at 20ºC: a) HH, b) HV, c) VH, d) VV polarized.

This figure shows that the Raman scatter band of water (O-H stretch, ~3400 cm^{-1}) is significantly stronger in the TSFS spectra collected in the VV orientation. The band corresponds to the Δλ ~45 nm feature that appears in the emission profiles extracted for Comp3, the weak RTP emission from Trp (Figure 2, main manuscript). To validate the band assignments from the MCR analysis of the *aniso*-TSFS data, we collected ARMES data from N-acetyl-tryptophan, N-acetyl-tyrosine, and mixtures of the two in a viscous solvent (Figure S-4).[1] This data was then analysed by MCR (Figure S-8)
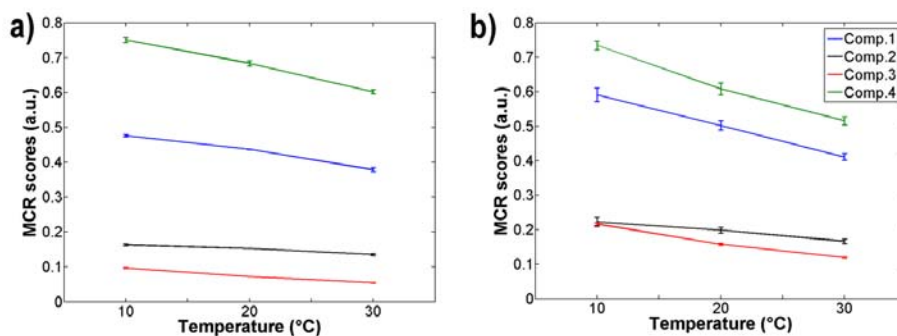

Figure S-8: MCR scores of pure components versus temperature plots: *a)* before and *b)* after deoxygenation, from HH polarized TSFS of HSA (1 mg mL^{-1}).

---

[1]   These derivatives were used because neither the pure Trp nor Tyr could be dissolved properly in the solvents used. Their emission properties are however very similar to the fluorophores as constituted in HSA.
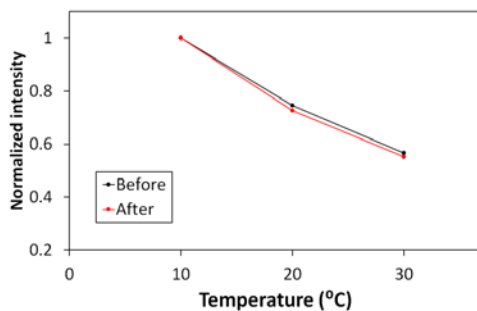
.

Figure S-9: Plot of the normalized MCR scores plots of component 3 (RTP) versus temperature. Plot shows the normalised values before and after deoxygenation for the HH polarized TSFS of HSA (1 mg mL^{-1}).
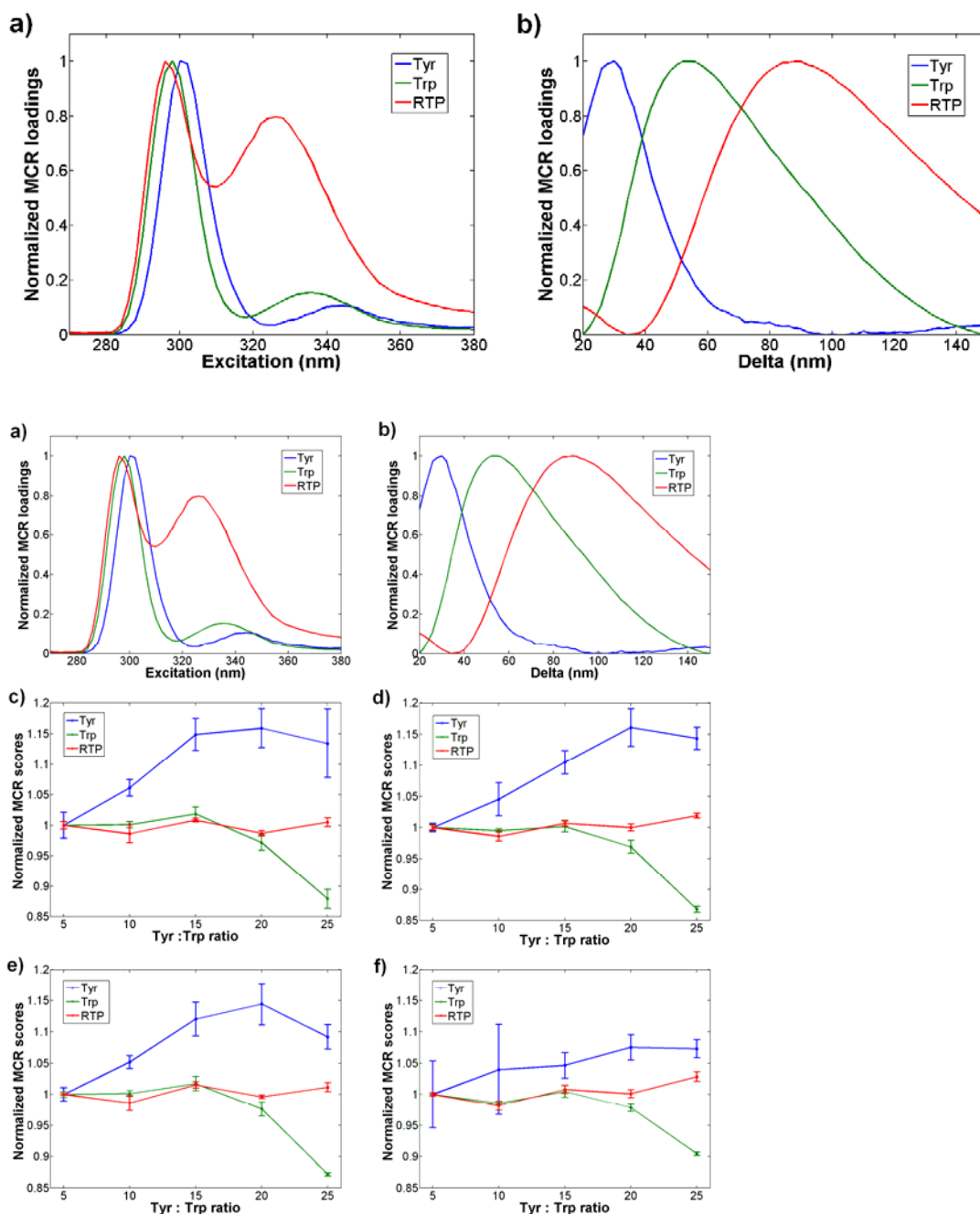
.

Figure S-10: (Top row) Normalized HH excitation and emission profiles of MCR model components for N-acetyl-Tyr and N-acetyl-Trp mixtures in 90% glycerol. (Middle & Bottom rows). Normalized MCR scores plots of pure components from a) HH, b) HV, c) VH and d) VV polarized datasets. Mixtures of N-acetyl-Tyr and N-acetyl-Trp in 90% glycerol were used with Tyr:Trp ratios from 5:1 to 25:1. N-acetyl-Trp concentration was maintained constant at 3.8×10^{-5}M

Table S-1: MCR model data fit for models with increasing number of components. This shows that 4 components was optimal in all cases.

Number of components	MCR model cumulative fit (%)			
	HH	VV	HV	VH
3	99.80	99.34	99.61	99.77
4	**99.89**	**99.63**	**99.73**	**99.86**
5	99.91	99.66	99.75	99.88
6	99.91	99.68	99.77	99.88

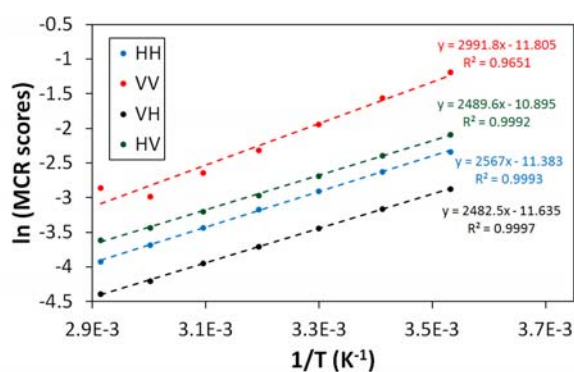## Monitoring thermal denaturation by ARMES

Figure S-11: Plot of ln(Comp3 MCR scores) versus 1/T for the 4 raw polarisation data sets. Plot shows good linearity except for the VV data where the highest temperature values deviate significantly from linearity.
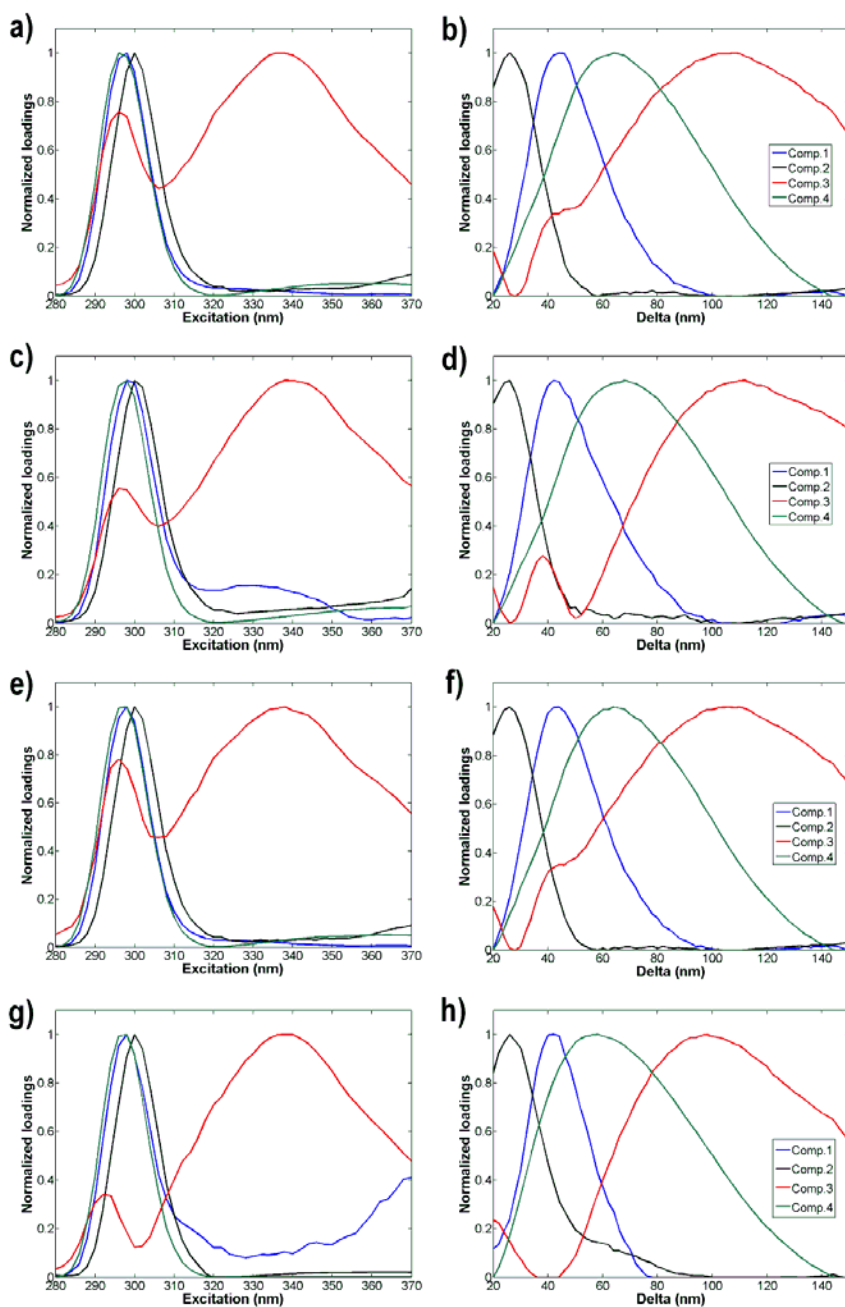
Figure S-12: Normalized excitation (left) and emission, Δλ (right) profiles of the MCR model components extracted from the HH (a/b), VV (c/d), VH (e/f), and HV (g/h) polarized fluorescence datasets recorded during the HSA chemical denaturation experiment.
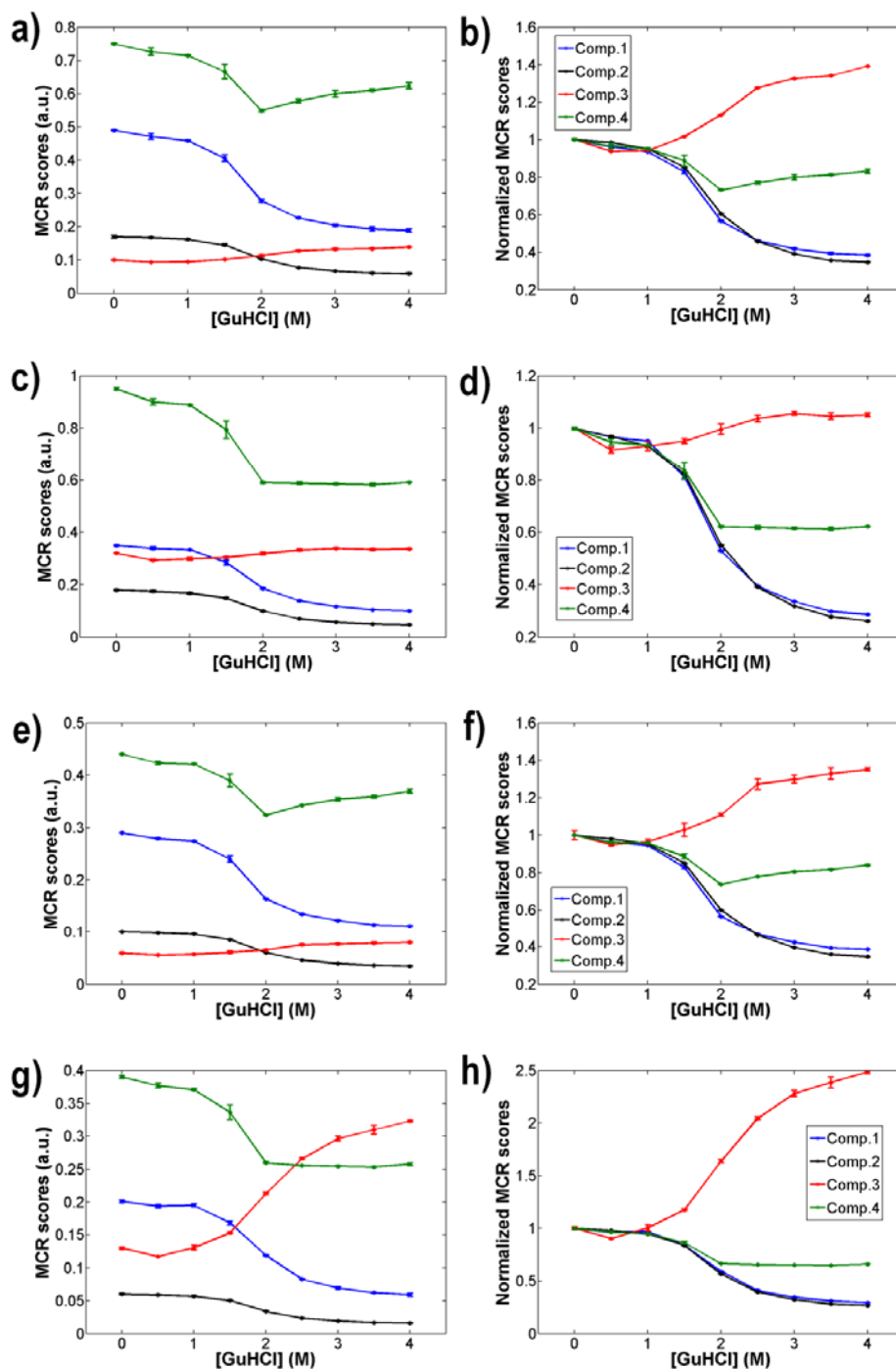
.

Figure S-13: MCR Scores plots and normalized MCR scores plots of pure components extracted from HH (a/b), VV (c/d), VH (e/f), and HV (g/h) polarized TSFS spectra of 1 mg mL^{-1} HSA in PBS undergoing chemical denaturation.